Eur. Phys. J. Plus (2024) 139:879
https://doi.org/10.1140/epjp/s13360-024-05672-4

THE EUROPEAN PHYSICAL JOURNAL PLUS

Regular Article

Advancing early detection of biological events by digital holographic microscopy and simulation of microorganisms

Alessandro Molani[1,a], **Béla Mihalik**[2], **Francesca Pennati**[1], **Praveen Rahi**[3], **Anna Mező**[4], **János Pálhalmi**[4], **Andrea Aliverti**[1], **Györgyi Bela**[2]

[1] Dipartimento di Elettronica, Informazione e Bioingegneria, Politecnico di Milano, Milan 20133, Italy
[2] Ideas Science Ltd., Budapest 1173, Hungary
[3] Institut Pasteur, Université Paris Cité, Biological Resource Center of Institut Pasteur - Collection de l'Institut Pasteur, Paris F-75015, France
[4] DataSenseLabs Ltd., Budapest 1068, Hungary

Received: 28 March 2024 / Accepted: 21 September 2024

Abstract There is a global need to advance bio-aerosol sensing for CBRN (Chemical, Biological, Radiological, and Nuclear) applications by compact and cost-effective devices. Employing digital holographic microscopy (DHM) and deep learning, we developed a system called HoloZcan to automate the analysis of airborne microbial pathogens and particles. DHM provides valuable information, but obtaining data from biological specimens for robust investigations is challenging. This paper introduces a custom simulation approach using the open-source software Meep and the finite-difference time-domain (FDTD) method to overcome limitations of existing Mie-based simulators, especially when dealing with complex microbial shapes. The simulation tool enables the modelling of specific microorganisms, offering a safer and more flexible alternative for CBRN research by bypassing ethical and logistical constraints associated with live pathogens. The study details the simulation workflow, built upon the construction of a database of optical properties of biological materials, for realistic simulations of light-microbe interactions. Evaluations on homogeneous and non-homogeneous objects demonstrate the tool's limited intrinsic errors and superior sensitivity to refractive index changes compared to traditional Mie-based simulations. This work significantly advances our capability to accurately simulate and analyse CBRN-related scenarios, enhancing comprehensive research in bio-aerosol sensing.

1 Introduction

The HoloZcan project, funded by the European Union, is a pioneering initiative aiming at increasing bio-aerosol sensing and measurement capability of Chemical, Biological, Radiological, and Nuclear (CBRN) practitioners. The primary objective is the development of a cost-effective and compact device, that combined with deep learning-assisted image processing techniques can automate the analysis of airborne pathogens and particles. The technology at the core of the HoloZcan device is digital holographic microscopy (DHM). DHM captures 3-dimensional information about specimens by recording the interference pattern between a reference light wave and the wave scattered by the sample [1]. Compared to conventional microscopy techniques, DHM quantitatively measures complex three-dimensional (3D) optical fields, by encoding both amplitude and phase information. The measured phase delay is directly related to the refractive index distribution of the sample [2], allowing optical properties and 3D characteristics to be obtained even for unstained transparent samples [3]. As the refractive index distribution is governed by the structural and chemical properties of the sample, holographic microscopy enables the simultaneous measurement of morphological, dynamical, and chemical feature related properties of cells [4].

However, the limited capability of achieving enough data for reliable investigations on biological specimens represents one of the obstacles for extensive research on current DHM concepts. In developing DHM for CBRN applications, there are critical cost and logistical challenges associated with preparing various biological materials for microscopic analysis. Furthermore, some pathogens and spores are not readily accessible for this kind of technology development and research involving live pathogens is subject to stringent ethical and regulatory constraints.

In this context, cell-level simulations play a crucial role. Simulations bypass many of these constraints, allowing for more flexible and extensive research while respecting ethical standards. Simulations provide a safer alternative, allowing for the study without the direct handling of dangerous pathogens. Working with simulated bacteria and other kind of cells enables researchers to manipulate and control various parameters, creating a controlled environment that is essential for accurate research. Mie-based simulators [5]

A. Molani and B. Mihalik have contributed equally to this work.

[a] e-mail: alessandro.molani@polimi.it (corresponding author)

Published online: 09 October 2024

allow accurate modelling of homogeneous spherical particles with high resolving power, based on the 3D coordinates of the sphere, on the radius of the particle, and on its refractive index. This approach has been extensively used for characterizing colloidal particles [6], measuring the dynamics of colloidal clusters [7] and for quantitatively tracking the motility of the bacteria *Escherichia coli* [8]. However, the applicability of these simulators is restricted when dealing with complex and irregular shapes, common in the context of biological particles.

Therefore, the aim of this study is to present a customised simulation procedure, tailored to overcome the current limitation of the Mie-based simulators. In particular, we implemented a DHM image simulator based on the finite-difference time-domain (FDTD) method [9], using the open-source software package Meep [10]. The simulator enables the implementation of complex structures, by allowing the modelling of specific microorganisms by defining shapes, sizes, and optical characteristics of its biological components. The driving motivation of the study is to enhance our ability to simulate and analyse CBRN-related scenarios more accurately than existing methods.

In the following paragraphs, we present the physics fundamentals of the developed simulator, and we detail both the design of the heuristic database of optical properties of biological materials, i.e., the fundamental component for achieving realistic simulations of the light-microbes interaction, and the simulation workflow. Finally, we evaluate the simulations of both homogeneous spherical objects, to investigate the tool sensitivity to small changes in refractive indexes compared to Mie-based simulations, and in non-homogeneous spherical objects, mimicking a generic spherical-shaped bacterium, or coccus, varying the size and the composition of its specific components.

2 Methods

2.1 Building the database of optical properties of biological materials

The first step to achieve realistic simulations of light propagation in a medium is the definition of a comprehensive database containing the optical properties of common biological materials. Locating the absorption and the scattering coefficients of each material in a look-up table, the corresponding refractive index is determined.

The refractive index (*RI*) is a characteristic parameter of a medium, which controls its interaction with light. Represented as a complex function, it has both real (n) and imaginary (κ) components:

$$RI = n + j\kappa \tag{1}$$

The real part n predominantly represents scattering, with the term "refractive index" commonly referring to this component alone. The imaginary part κ is the optical extinction coefficient and is an indicator of the absorption of the incident optical field within the medium [11].

As the real and imaginary components of *RI* are indicative of the scattering and absorption coefficients of the medium, *RI* is the fundamental optical parameter of cellular and molecular structures. In fact, the light interaction with microorganisms is closely linked to the spatial distribution of the complex refractive index and the morphological parameters that characterize these biological entities [11]. In this context, label-free imaging methodologies, like DHM, leverage the complex refractive index distribution to extract information without the need for contrast agents or stains. This is particularly advantageous in biological studies, where maintaining the natural state of cells or tissues is crucial.

The importance of this parameter makes it a key element for simulations of microorganisms. *RI* strongly depends on the light wavelength, a phenomenon named chromatic dispersion. A well known and simple index describing the chromatic dispersion of transparent materials in the visible wavelength range is the Abbe number. The Abbe number (v_d) is defined as $v_d = (n_d - 1)/(n_F - n_C)$, where n_d is the refractive index at 587.56 nm (*He*-line, Fraunhofer's symbol *d*), n_F is the refractive index at 486.13 nm (H_β-line, Fraunhofer's symbol *F*), and n_C is the refractive index at 656.27 nm (H_α-line, Fraunhofer's symbol *C*). Unfortunately, for biological materials, the Abbe number is mostly missing. Therefore, the wavelength dependence of the refractive index of each biomaterial was approximated by assigning chromatic dispersion values to the material at 587.56 nm and by using a second-order approximation of the Cauchy model:

$$n(\lambda) = A + \frac{B}{\lambda^2} \tag{2}$$

where A and B are the model coefficients at specific wavelengths λ. The local dispersion coefficient ($dn/d\lambda$) at $\lambda = 587.56$ nm is equal to -9.83 when $B = 1$, which we approximated to 10, as the local dispersion coefficient ranges from an order of magnitude lower, to an order of magnitude larger, than that calculated for $B = 1$. With this approximation, model coefficients can be calculated with the following formulas:

$$B = -n_0 \frac{C D_0}{10} \tag{3}$$

$$A = n_0 - \frac{B}{\lambda_0^2} \tag{4}$$

Table 1 Database of optical properties of biological components. Chromatic dispersion (CD_0) and refractive index (n_0) at the specified wavelength (λ_0) are reported for some example materials. A literature source discussing the values obtained is indicated

Material	λ_0 [μm]	n_0	CD_0 [μm^{-1}]
Vacuum	0.50	1.00	0.00
Air [12]	0.59	1.00	0.00
Water [12]	0.59	1.33	−0.04
DNA [12]	0.59	1.58	−0.08
RNA [13]	0.59	1.51	−0.10
Carbohydrates [14]	0.59	1.53	−0.01
Proteins [15]	0.59	1.58	−0.10
Lipids [16]	0.53	1.50	−0.10
Phospholipids [17]	0.53	1.44	−0.10
Ions (KCl, NaCl) [12]	0.50	1.50	−0.10

where CD_0 is the chromatic dispersion of material at wavelength λ_0, near the Fraunhofer's d wavelength and n_0 is the corresponding refractive index. Due to the limits of applicability of Cauchy's equation, the values of refractive index have been calculated in the spectral range from 200 nm to 1000 nm and cosine interpolation was used to converge to calculated limits. With this approximation the model can mimic the exponential characteristics of optical property in the visual domain, while maintaining smooth approach of limit values in near ultraviolet (UV) and infrared (IR) regions. In Table 1, the values of λ_0, n_0, and CD_0 for some of the biological components in our database are reported.

Similarly, the absorption coefficients were determined using the Beer-Lambert law. Absorption coefficients are related to κ by:

$$\alpha = \frac{4\pi\kappa}{\lambda} \tag{5}$$

Although measured values of RI strongly depend on various experimental conditions, including temperature, chemical treatments, sample preparation processes, osmotic pressure, life cycle, as well as unpredictable chaotic processes [18], the database represents a reasonable approximation as it was designed to simulate the influence of specific factors on the outcomes, rather than completely matching actual measurements.

2.2 DHM image simulator

The DHM image simulator relies on the open-source software package Meep [10] which employs the FDTD method [9]. The FDTD method is a numerical technique used for solving partial differential equations (PDEs) and, in the context of electromagnetic wave propagation, it is used to divide space and time into a regular grid (Yee grid) and simulate the time evolution of Maxwell's equations [10]. The implementation in Meep involves specifying the geometry, material properties, and boundary conditions of the simulation domain.

2.2.1 Defining the simulation scenario

The first part of the computation consists in the definition of the simulation scenario setting the attributes required for the Meep simulation based on the user-defined input parameters. The simulation parameters can be defined as command line arguments. These attributes include:

- the simulation space and resolution,
- the boundary conditions,
- the light source,
- the object geometry and optical properties.

The parameters provided by the user include the pixel size to define the simulation resolution, the simulation space dimensions, the thickness of the perfectly matched layer (PML), and the wavelength (λ) of an unpolarized continuous light source. The PML is a special boundary condition to limit the simulation to a finite region. It emulates a fictious material which absorbs outgoing electromagnetic waves and minimizes reflections [19]. Additionally, through Meep, the simulator allows the definition of 2D and 3D parametric morphological models of complex geometric structures composed of different materials and shapes. To model a microorganism, the simulator can receive input in the form of a text file containing the description of the microbe of interest. This description delineates the properties of various cellular structures, detailing their number, size, shape, and composition in terms of the biological components listed in Table 1, and optionally, their volume fractions (Fig. 1). Table 2 shows a list of implementable structures within the simulator, along with their respective significance [20].

Based on the specified properties, a microorganism object is constructed, assembling the cellular structures into a unified Meep object. For each cellular structure, the morphological properties are converted to shapes and sizes. Concerning optical characteristics,

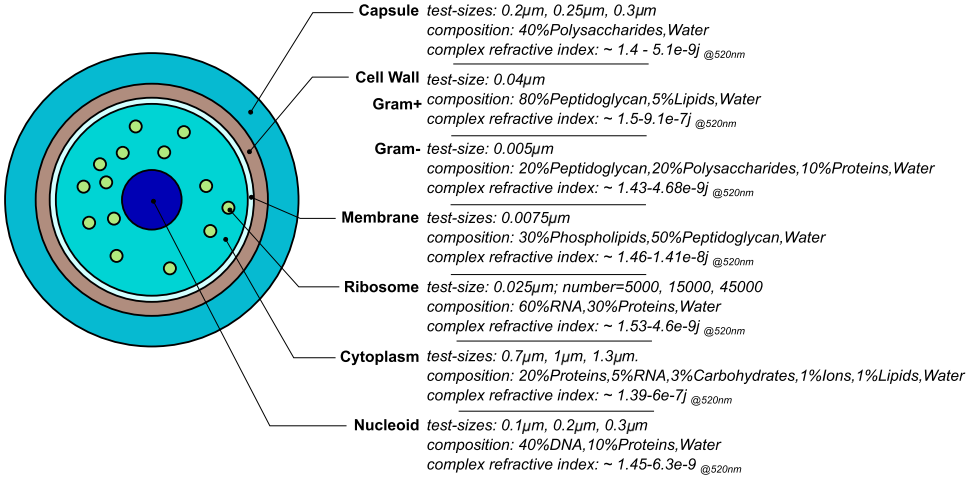

Fig. 1 Parametric morphological model of a simulated microorganism. Size and material composition of the different organelles and structures are parameters given as input to the simulation algorithm

Table 2 List and description of some implemented structures [20]

Bacteria	
Nucleoid	Region in prokaryotic cells (bacteria and archaea) where genetic material (DNA) is located. Unlike eukaryotic cells, prokaryotes lack a membrane-enclosed nucleus.
Ribosomes	Cellular structures composed of RNAs and proteins responsible for new protein synthesis. They can be found free in the cytoplasm or attached to the endoplasmic reticulum.
Cytoplasm	Fluid portion of a cell, bounded by the cell membrane. It contains organelles.
Plasma membrane	Semipermeable barrier that separates the cell interior (cytoplasm) from the environment. It is a phospholipid bilayer and regulates the passage of molecules in and out of the cell.
Cell wall	Rigid layer outside the cytoplasmic membrane that confers structural strength on the cell and protection. Found in plant cells and most microorganisms, not in animal cells, with rare exceptions.
Capsule	Dense, well-defined polysaccharide or protein layer closely surrounding a cell.

the cellular structure complex *RI* is computed as the weighted sum of the complex *RI* of its biological components (Table 1) and their respective volume fractions. The refractive index (n) and absorption coefficient (α) of each component are retrieved from the database for the specified wavelength. In cases where the wavelength of interest is not specified, values are interpolated based on the nearest wavelengths available in the database. The interpolation of n uses a cosine function, while the absorption coefficient α undergoes cosine and logarithmic interpolation before conversion to the optical extinction coefficient. Finally, the cellular structure complex *RI* is transformed into a Meep material object. Considering only the wavelength of interest, this is handled by Meep by specifying the frequency-independent dielectric constant $\epsilon_\infty = n^2$ and electric conductivity $\sigma_D = 2\pi f \frac{\kappa^2}{n^2}$, where n and κ are the real and imaginary part of the complex refractive index, while $f = 1/\lambda$, where λ is the simulation wavelength.

Utilizing the same approach, the simulator also allows placing the object to be simulated on a glass plate. In fact, the database incorporates not only the optical properties of biological components, but also those of other materials, including glass. In this scenario, light is first propagated from the glass to the air, causing reflections and possible changes in the scattering profiles. This capability further enhances the simulator's adherence to reality by mimicking the actual observation process under a microscope.

2.2.2 Running the simulation

After the parameters' definition, the simulation is initiated and runs until a stop condition is met. This condition is determined by the number of iterations, which is calculated from the parameters defining the geometry of the object and the simulation space. At each step, the updated values for the electric and magnetic fields are calculated at each point in the simulation space.

The simulation is run for two distinct scenarios: "empty", denoting the absence of any object or microorganism, and "object", representing the presence of an object or microorganism. The importance of this step is twofold. First, it facilitates the assessment for potentially non-negligible errors from the simulation approximations and procedures. Second, it enables the extraction of the object-specific scattering amplitudes by dividing the overall scattering data by the simulated empty field data, thus isolating and characterising the contribution attributable to the presence of the object or microorganism alone.

To determine the fields, the single frequency Discrete Fourier-Transformed (DFT) electric (E) and magnetic (H) fields are computed over the defined simulation volume for both scenarios and stored as tensors. The magnitudes of E and H at each spatial point in the array are calculated separately, taking the square root of the sum of the squared components summed along the last

dimension. The magnitude of the Poynting vector (S) is obtained by multiplying the magnitudes of the electric and magnetic fields at each spatial point, assuming a non-magnetic condition ($\mu = 1$). This magnitude represents the intensity of the electromagnetic field at those points.

$$S = \frac{1}{\mu} E H \tag{6}$$

2.2.3 Simulation results extraction and visualization

The material map and the intensity fields are extracted from the simulation results and visualized. The material map is the graphical representation of the material or dielectric constant spatial variation in the simulation cell. The intensity fields represent the intensity distribution for the two scenarios, that is the intensity distribution within free space ("empty"), which should only be affected by the choice of the PML layer, and the intensity distribution caused by the object ("object"). The object intensity distribution is corrected by dividing it by the "empty" intensity, excluding the contribution of the background signal and isolating the effect of the object.

2.3 Simulator evaluation

2.3.1 Evaluation process

To evaluate the simulator performance, we conducted a comparative analysis of the "empty" and "object" fields characteristics. We considered the simulation volume excluding the PML layer. The resulting volumes were normalized by their mean values and expressed as percentages. As with data visualization, the object volume was corrected by dividing it by the empty volume. This mitigates the influence of the empty field, allowing for a focused analysis of the properties specific to the object. Statistical parameters, including mean, standard deviation, and peak-to-peak values, were computed for the volumes of the "empty", "object", "corrected" and "correction" field, the latter being the difference between the non-corrected and the corrected object volume. Additionally, the same metrics were applied to the hologram planes extracted from the aforementioned volumes. We calculated the percentage ratio between the peak-to-peak amplitudes of the corrected object's fields to those of the empty field as an estimate of the signal-to-noise ratio.

2.3.2 Simulated holograms of homogeneous microspheres

In the assessment of the simulator's applicability to CBRN applications, we first examined the scenario of a homogeneous sphere. We considered a non-absorbing spherical particle in air ($n = 1$) with a diameter of 1 μm, which is the mean diameter of a spherical-shaped bacterium, positioned at an axial distance of $z = 2.5$ μm. The simulation parameters included a 50 nm pixel size, 5 μm simulation space, 0.5 μm PML, and an unpolarized incident light at a wavelength of $\lambda = 520$ nm. To mimic biological entities, we set the real component of the refractive index to that of bacteria ($n = 1.4$) [21]. We compared holograms generated by our proposed FDTD-based simulator with those produced by different implementations of Mie simulators, specifically HoloPy and miepython, under equivalent conditions. HoloPy is a Python library for light scattering and digital holograms [22], and miepython is a Python module for calculating light scattering using Mie theory [23]. The simulations involved spheres with the same conditions but with refractive index differences (ΔRI) of 1% and 1‰. Absolute differences in the generated holographic profiles (i.e., pixel values along the horizontal line passing through the hologram centre) were quantified for each simulator. To account for possible differences in scales adopted by the simulators, we applied min-max rescaling to the intensity profiles. In the instance of analysing simulated pixel intensity profiles, the minimum relevant variation in *RI* should be 0.01 to be identified by statistical methods. Variations of this magnitude have indeed been observed in various microorganisms and cellular structures of interest. For instance, the distribution of *RI* values in the sporulated and vegetative forms of *Bacillus cereus* ranges from 1.517 to 1.539 and 1.387 to 1.400, respectively [24]. Similarly, the mitochondrial *RI* distribution falls between 1.400 and 1.420 [25], while the *RI* range for the cytoplasm and nucleoid is found to be between 1.390 and 1.371 [26].

2.3.3 Simulated holograms of microbes

To demonstrate the versatility of the simulator, we performed simulations focused on generating holographic images of a non-homogeneous object while systematically varying specific characteristics. The composition of this spherical object mimics that of a bacterium, specifically a generic coccus. The baseline composition of the microbe (Gram positive), along with the systematically varied size and composition parameters, is detailed in Table 3.

This series of simulations aimed to assess the simulator's ability to produce different holograms in response to parameter changes and to measure the extent of these variations. For this latter purpose, we computed the structural similarity index (SSI) to assess the similarities between the images of the generated holograms. The SSI quantifies the structural resemblance between two images, providing a numerical value ranging from -1 (complete dissimilarity) to 1 (perfect similarity). The simulations were conducted at

Table 3 Simulated bacteria composition and applied variations. Composition, size in micrometre, and number of elements (N) are reported for each structure

Structure	Baseline composition (Gram positive)	Variation
Nucleoid	40% DNA, 10% Proteins, Water – 0.2 μm	0.1–0.3 μm
Ribosomes	60% RNA, 30% Proteins, Water – 0.025 μm – N = 15000	N = 500–45000
Cytoplasm	20% Proteins, 5% RNA, 3% Carbohydrates, 1% Ions, 1% Lipids, Water – 1 μm	0.7–1.3 μm
Membrane	30% Phospholipids, 50% Peptidoglycan, Water – 0.0075 μm	–
Wall	80% Peptidoglycan, 5% Lipids, Water – 0.04 μm	Gram negative: 20% Peptidoglycan, 20% Polysaccharides, 10% Proteins, Water
Capsule	40% Polysaccharides, Water – 0.25 μm	0.2–0.3 μm

a wavelength of 520 nm, with a simulation space size of 4 μm, and a PML of 0.5 μm. A pixel size of 20 nm was chosen to ensure the inclusion of very small structures, such as ribosomes, in the holographic images.

3 Results

3.1 Evaluation process

For the simulation of the baseline coccus, the peak-to-peak amplitude of the empty field was observed to be as low as 4.5% both in the overall volume and in the hologram plane. This minimal error suggests a negligible intrinsic propagation error in the algorithm. Moreover, the standard deviation of the empty field is 0.3% in the overall volume and 0.7% in the hologram plane, indicating a homogeneous empty field, which is desirable. Despite their minimal values, these errors are taken into account in the simulation workflow by initially running the propagation in the empty field, and then using the results to correct the object field, eliminating their contribution. In relation to the signal range associated with the microscopic object, the peak-to-peak error-to-signal ratio is as low as 0.001% in the volume and 0.02% in the hologram plane. Such a small error implies that the object signal is highly discernible over the background. Comparable values are obtained for the simulation of the homogeneous 1 μm sphere. It has to be noted that the accuracy of the results in FDTD methods is related to the choice of an adequately small pixel size. In fact, the pixel size must be at least 8 times smaller than the smallest wavelength of the propagated light of interest in the material with the highest refractive index [27]. This implies that also the errors, as we have calculated, tend to decrease as the pixel size decreases.

3.2 Simulated holograms of homogeneous microspheres

The holograms generated by the different simulators for the 1 μm non-absorbing spherical particle ($n = 1.4$) are shown in Fig. 2a. The normalized intensity profiles for particles with refractive indices $n = 1.4$ and $n = 1.41$, obtained with the different simulators, are reported in Fig. 2b. The absolute differences in the hologram profiles (Fig. 2c) for the same simulator suggest that, under equivalent conditions, for the same ΔRI, our proposed Meep FDTD-based simulator captures more variations in the simulated holograms compared to Mie simulators. With $\Delta RI = 1‰$, the observed variations in intensity profiles are on the order of magnitude of 10^{-3}. However, even in this case, a greater variation in the intensity profile is observed with the proposed simulator. The increased sensitivity of our Meep FDTD-based simulator suggests a potential advantage in characterizing and identifying biological particles with distinct optical properties, as the simulator enables a more precise characterization of subtle variations in refractive index.

3.3 Simulated holograms of microbes

Figure 3 shows the intensity profiles of holograms generated by our FDTD-based simulator, each corresponding to a tested variation in bacterial composition, according to Table 3.

The generated holograms and corresponding intensity profiles for each variation are reported in Online Resource (Figure S1 through S5). A qualitative analysis of these profiles suggests that some induced parameter changes have a more pronounced impact on the hologram's morphology, both concerning the central peak intensity (e.g., the number of ribosomes) and the interference fringes. To quantitatively assess these differences, SSI values were computed and are detailed in Table 4.

The SSI values for capsule size, cell wall composition ("Gram"), nucleoid size, and number of ribosomes suggest varying degrees of similarity, with changes in nucleoid size exhibiting the highest similarity (0.9971), and those in capsule size the lowest (0.5238). The negative SSI value for the holographic images of bacteria simulated with different cytoplasm dimensions (−0.05097) indicates a strong dissimilarity in holographic structures associated with size variations.

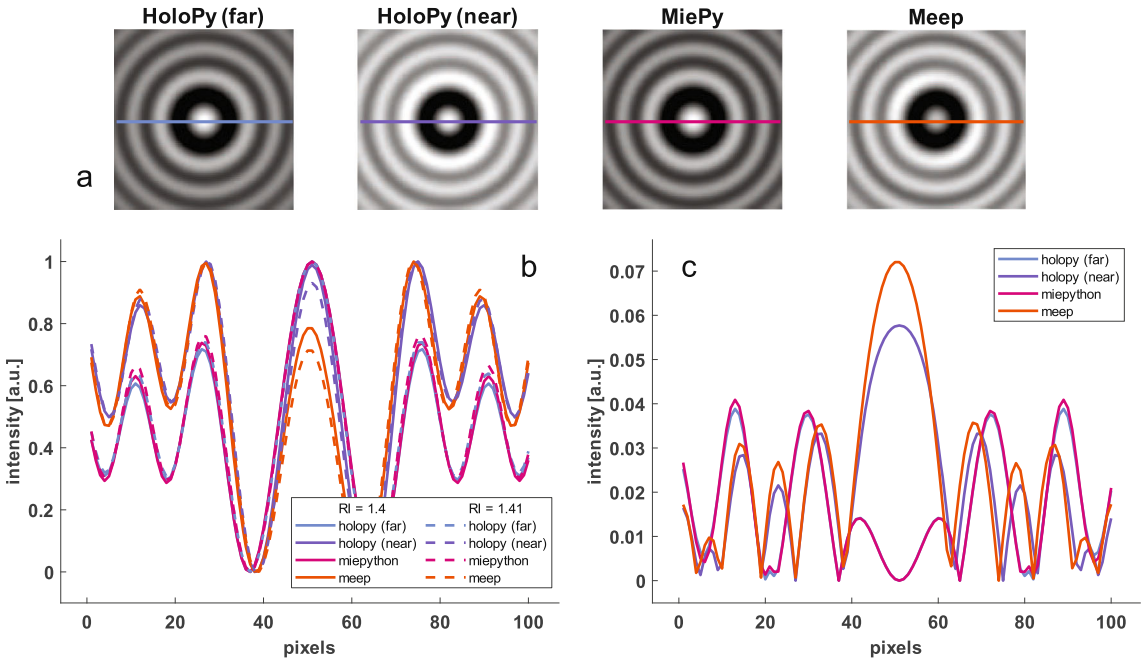

Fig. 2 **a** Holograms generated by the different simulators for a 1 μm non-absorbing spherical particle ($n = 1.4$) in air ($n = 1$), at an axial distance $z = 2.5$ μm, considering a 50 nm pixel size, an unpolarized incident light at $\lambda = 520$ nm, and 5 μm simulation space. 0.5 μm PML is used in Meep.**b** The intensity profiles are the pixel values along the coloured lines in (a). Different line colours represent the results obtained with the different simulators. Solid lines correspond to $RI = 1.4$. Dashed lines correspond to $RI = 1.41$.**c** Absolute values of the differences between the intensity profiles with $RI = 1.4$ and $RI = 1.41$

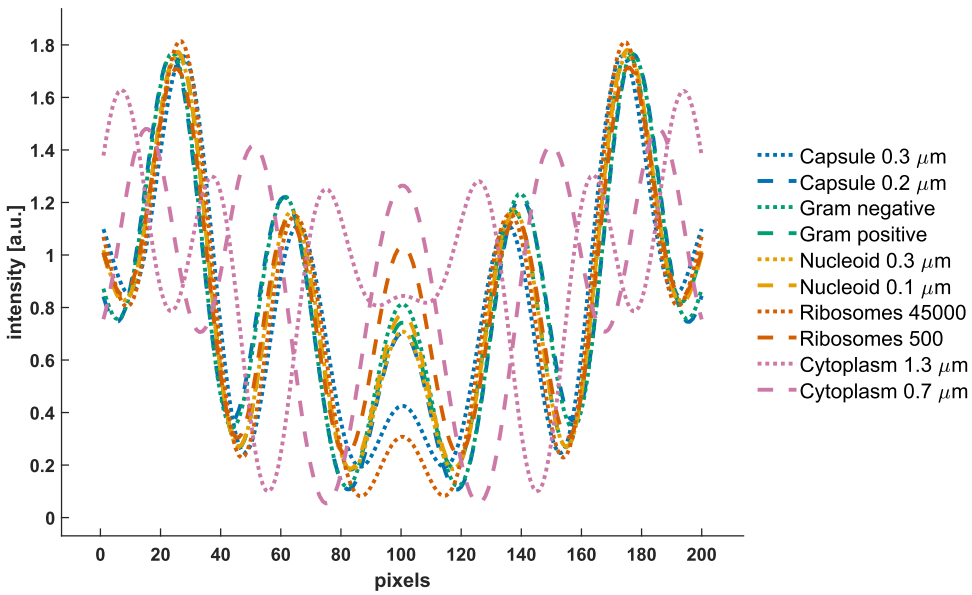

Fig. 3 Intensity profiles of holograms generated by the proposed simulator, each simulation highlighting the modification of a single parameter in the bacterial composition, according to Table 3. Light wavelength $\lambda = 520$ nm, pixel size $px = 20$ nm, axial distance $z = 2.5$ μm, 4 μm simulation space with 0.5 μm PML

4 Discussion

The results of this study, which cannot be explored using conventional Mie simulators, offer insights into investigating the theoretical limits of the simulator and gaining a deeper understanding of how various microbiological characteristics influence the holographic microscopy images. Further analyses are required to delve into these aspects, and future studies can compare the simulator's adherence to reality by appropriately modifying the parameters.

Given the importance of the *RI* parameter and its variability within different conditions and biological structures, the optical property database could be refined and expanded. While the current approximations are reasonable, there is room for improvement by incorporating more detailed information and values specific to certain conditions, such as temperature and sample preparation processes. Employing more precise models like the Sellmeier equation [28] could enhance the accuracy of the wavelength-refractive

Table 4 Variated structures and structural similarity index (SSI) between the resulting holographic images

Structure	SSI
Capsule	0.5238
Gram	0.8234
Nucleoid	0.9971
Ribosomes	0.8731
Cytoplasm	−0.05097

index relationship. Additionally, the definition and characterization of cellular and subcellular structures in bacteria, particularly those relevant in CBRN scenarios like endospores from bacterial pathogens, can be further refined.

Expanding the capabilities of the simulator also involves refining the representation of rod-shaped bacteria, or bacilli, and incorporating nonlinear effects into the analysis. Currently approximated as ellipsoids, bacilli could have a more precise implementation of their rod-shaped structure within the simulator. This adjustment would improve the accuracy of the simulations and contribute to a more realistic representation. Additionally, extending the simulator to calculate nonlinear effects would make the simulation of the microbe autofluorescence spectrum possible. In fact, the material database contains absorption coefficients from ultraviolet B (UVB) to near infrared (NIR). By storing the absorbed values during the simulation and combining this information with the knowledge of the material, the emitted light can be calculated. Propagating this fluorescent light through the cell and considering the processes of reabsorption and re-emission would enable the estimation of the microbe final spectrum. Leveraging the recorded fluorescent spectra of common pathogens for model calibration could enhance the alignment of simulated results with real measurements, providing a valuable framework for understanding the limitations and potential advancements in fluorescent spectrum-based classifications.

Another important aspect for consideration is the computational efficiency of the simulator. The pixel size significantly influences computation time, while providing the capability to capture subtle variations. Currently, simulations of 1 μm spherical particles with a 50 nm pixel size take approximately 1 min, increasing to about 20 min for more complex structures simulated with a 20 nm pixel size, on a 12th Gen Intel(R) Core(TM) i7-12700 H 2.70 GHz personal computer. Ongoing efforts to implement a faster simulator based on layer-by-layer propagation are already underway.

Future work should involve a systematic comparison of different simulators, evaluating their strengths and limitations under various conditions. This comparative analysis will contribute to a better understanding of each simulator's performance and aid researchers in choosing the most suitable tool for specific applications.

While any modelling approach involves a degree of inaccuracy, the comparison of simulator results with real measurements is crucial. This could be performed in terms of signal trends. This comparison would contribute significantly to bridging the gap between computational simulations and real-world scenarios. It is important to note as well that the small pixel sizes utilized in this study serve the purpose of exploring theoretical limits. To understand practical limitations and facilitate the comparison of simulation results with real measurements, a larger pixel size would be necessary.

The current version of the simulator provides a range of analysis possibilities. Modelling of organelles for microorganisms other than bacteria is already implemented, featuring structures including nucleus, nucleolus, endoplasmic reticulum, lysosomes, Golgi apparatus, mitochondria for eukaryotes, and capsid and envelope for viruses. In the CBRN field, relevant simulations could include, for instance, comparing bacteria within the same genus but different species, and contrasting the vegetative cell form with the endospore form. Endospores are structures extremely resistant to heat, harsh chemicals, and radiation produced by specific bacterial species, in particular from the genus *Bacillus*. While some *Bacillus* species, like *B. subtilis*, are considered safe for health, *B. anthracis* is classified as a Category A agent for biowarfare and bioterrorism. *B. anthracis*'s endospores, resistant to heat and drying, increase the ability of this bacterium to spread in aerosols, being easily dispersed by the wind. Structurally, the endospore is more complex than the vegetative cell, featuring additional layers such as the exosporium, spore coats, and cortex. Moreover, the core of a mature endospore undergoes dehydration during sporulation, retaining only 10–25% of the water content found in the vegetative cell [20].

The simulator allows these scenarios to be simulated and studied, offering a safe and ethically acceptable means of analysis without the need to handle hazardous pathogens. Finally, the simulator can be used for studies beyond the CBRN field, like diagnosis or air monitoring, among others. This not only contributes to our scientific understanding of light-microbe interactions, but it is also promising to enhance the practical applications of DHM in safeguarding against potential threats in bioaerosol dispersion-based scenarios.

5 Conclusion

In conclusion, this paper presented a custom holographic image simulation approach aimed at using DHM for bio-aerosol sensing in CBRN applications. The simulator, based on the FDTD method within Meep software, has the key advantage of simulating complex 3D structures and models of microorganism, mimicking realistic representations of various scenarios. Customized models with

user-defined attributes and a comprehensive database of optical material properties enhance the simulator's potential. The simulator algorithm is characterized by limited intrinsic errors and superior sensitivity to refractive index changes compared to traditional Mie-based simulations. While acknowledging the achievements, areas for improvement include refining the optical properties and geometries, considering nonlinear effects, and addressing computational efficiency. Overall, the simulator is a valuable and versatile tool for advancing research on bio-aerosol sensing for CBRN applications in a controlled environment.

Supplementary Information The online version contains supplementary material available at https://doi.org/10.1140/epjp/s13360-024-05672-4.

Acknowledgements The authors would like to thank Mariana Ferrari for critical reading of the manuscript and constructive remarks, and the UTechS Photonic Bioimaging platform of C2RT of Institut Pasteur, in particular Nathalie Aulner and Julien Fernandes, for hosting the HoloZcan prototypes and for their input and technical support.

Funding Open access funding provided by Politecnico di Milano within the CRUI-CARE Agreement. This project has received funding from the European Union's Horizon 2020 research and innovation programme, under grant agreement No 101021723.

Data Availability Statement This manuscript has associated data in a data repository. The data supporting the findings of this study are available within the paper and its Supplementary Information should any raw data files be needed they are available from the corresponding author upon reasonable request.

Declarations

Conflict of interest The authors have no relevant financial or non-financial interests to disclose.

References

1. M.K. Kim, Principles and techniques of digital holographic microscopy. Journal of Photonics for Energy p. 018005 (2010). doi:10.1117/6.0000006
2. J. Birdi, S. Rajora, M. Butola, K. Khare, True 3D reconstruction in digital holography. Journal of Physics: Photonics **2**, 044004 (2020). https://doi.org/10.1088/2515-7647/abb586
3. B. Rappaz, B. Breton, E. Shaffer, G. Turcatti, Digital holographic microscopy: A quantitative label-free microscopy technique for phenotypic screening. Combinatorial Chemistry & High Throughput Screening **17**, 80–88 (2014). https://doi.org/10.2174/13862073113166660062
4. G. Popescu, Y. Park, N. Lue, C. Best-Popescu, L. Deflores, R.R. Dasari, M.S. Feld, K. Badizadegan, Optical imaging of cell mass and growth dynamics. American Journal of Physiology-Cell Physiology **295**, C538–C544 (2008). https://doi.org/10.1152/ajpcell.00121.2008
5. C.F. Bohren, D.R. Huffman, *Absorption and Scattering of Light by Small Particles* (John Wiley & Sons, Ltd, Weinheim, 1998), pp. 82–129. doi:10.1002/9783527618156
6. S.H. Lee, Y. Roichman, G.R. Yi, S.H. Kim, S.M. Yang, A. van Blaaderen, P. van Oostrum, D.G. Grier, Characterizing and tracking single colloidal particles with video holographic microscopy. Optics Express **15**, 18275 (2007). https://doi.org/10.1364/OE.15.018275
7. J. Fung, K.E. Martin, R.W. Perry, D.M. Kaz, R. McGorty, V.N. Manoharan, Measuring translational, rotational, and vibrational dynamics in colloids with digital holographic microscopy. Optics Express **19**, 8051 (2011). https://doi.org/10.1364/OE.19.008051
8. A. Wang, R.F. Garmann, V.N. Manoharan, Tracking E. coli runs and tumbles with scattering solutions and digital holographic microscopy. Optics Express **24**, 23719 (2016). doi:10.1364/OE.24.023719
9. A. Taflove, A. Oskooi, S. Johnson, *Advances in FDTD Computational Electrodynamics: Photonics and Nanotechnology* (Artech House Inc, Norwood, MA, 2013)
10. A.F. Oskooi, D. Roundy, M. Ibanescu, P. Bermel, J. Joannopoulos, S.G. Johnson, Meep: A flexible free-software package for electromagnetic simulations by the FDTD method. Computer Physics Communications **181**, 687–702 (2010). https://doi.org/10.1016/j.cpc.2009.11.008
11. R. Khan, B. Gul, S. Khan, H. Nisar, I. Ahmad, Refractive index of biological tissues: Review, measurement techniques, and applications. Photodiagnosis and Photodynamic Therapy **33**, 102192 (2021). https://doi.org/10.1016/j.pdpdt.2021.102192
12. M.N. Polyanskiy, Refractiveindex.info database of optical constants. Scientific Data **11**, 94 (2024). doi:10.1038/s41597-023-02898-2
13. M. Ghasemi, H. Jeong, D. Kim, B. Kim, J.I. Jang, K. Oh, Linear and nonlinear optical properties of transfer ribonucleic acid (tRNA) thin solid films. RSC Advances **12**, 8661–8667 (2022). https://doi.org/10.1039/D1RA09412B
14. G.T. Keenan, The optical properties of some sugars. Journal of the Washington Academy of Sciences **16**(16), 433–440 (1926). http://www.jstor.org/stable/24529384
15. D. Fu, W. Choi, Y. Sung, Z. Yaqoob, R.R. Dasari, M. Feld, Quantitative dispersion microscopy. Biomedical. Optics Express **1**, 347 (2010). https://doi.org/10.1364/BOE.1.000347
16. S. Johnsen, E.A. Widder, The physical basis of transparency in biological tissue: Ultrastructure and the minimization of light scattering. Journal of Theoretical Biology **199**, 181–198 (1999). https://doi.org/10.1006/jtbi.1999.0948
17. M.C. Howland, A.W. Szmodis, B. Sanii, A.N. Parikh, Characterization of physical properties of supported phospholipid membranes using imaging ellipsometry at optical wavelengths. Biophysical Journal **92**, 1306–1317 (2007). https://doi.org/10.1529/biophysj.106.097071
18. B. Gul, S. Ashraf, S. Khan, H. Nisar, I. Ahmad, Cell refractive index: Models, insights, applications and future perspectives. Photodiagnosis and Photodynamic Therapy **33**, 102096 (2021). https://doi.org/10.1016/j.pdpdt.2020.102096
19. S.G. Johnson, Notes on perfectly matched layers (PMLs) (2021). arXiv:2108.05348
20. M.T. Madigan, J.M. Martinko, D.A. Stahl, D.P. Clark, *Brock Biology of Microorganisms*, 13th edn. (Pearson Education, 2010)

21. P.Y. Liu, L.K. Chin, W. Ser, H.F. Chen, C.M. Hsieh, C.H. Lee, K.B. Sung, T.C. Ayi, P.H. Yap, B. Liedberg, K. Wang, T. Bourouina, Y. Leprince-Wang, Cell refractive index for cell biology and disease diagnosis: past, present and future. Lab on a Chip **16**, 634–644 (2016). https://doi.org/10.1039/C5LC01445J
22. S. Barkley, T.G. Dimiduk, J. Fung, D.M. Kaz, V.N. Manoharan, R. McGorty, R.W. Perry, A. Wang, Holographic microscopy with Python and HoloPy. Computing in Science & Engineering **22**, 72–82 (2020). https://doi.org/10.1109/MCSE.2019.2923974
23. S. Prahl. miepython: Pure python implementation of mie scattering (2023). doi:10.5281/zenodo.8218010
24. K.F.A. Ross, E. Billing, The water and solid content of living bacterial spores and vegetative cells as indicated by refractive index measurements. Journal of General Microbiology **16**, 418–425 (1957). https://doi.org/10.1099/00221287-16-2-418
25. K. Haseda, K. Kanematsu, K. Noguchi, H. Saito, N. Umeda, Y. Ohta, Significant correlation between refractive index and activity of mitochondria: single mitochondrion study. Biomedical Optics Express **6**, 859 (2015). https://doi.org/10.1364/BOE.6.000859
26. J.A. Valkenburg, C.L. Woldringh, Phase separation between nucleoid and cytoplasm in Escherichia coli as defined by immersive refractometry. Journal of Bacteriology **160**, 1151–1157 (1984). https://doi.org/10.1128/jb.160.3.1151-1157.1984
27. D.E. McCoy, A.V. Shneidman, A.L. Davis, J. Aizenberg, Finite-difference Time-domain (FDTD) optical simulations: a primer for the life sciences and bio-inspired engineering. Micron **151**, 103160 (2021). https://doi.org/10.1016/j.micron.2021.103160
28. J.W. Gooch, *Cauchy's Equation* (Springer New York, New York, NY, 2011), pp. 125–125. doi:10.1007/978-1-4419-6247-8_2057